Journal of the Korean Astronomical Society
50: 157 ∼ 165, 2017 December

https://doi.org/10.5303/JKAS.2017.50.6.157
pISSN: 1225-4614 · eISSN: 2288-890X
http://jkas.kas.org

Time Variations of the Radial Velocity of H_2O Masers in the Semi-Regular Variable R Crt

Hiroshi Sudou[1], Motoki Shiga[†1,2], Toshihiro Omodaka[3], Chihiro Nakai[3], Kazuki Ueda[1], and Hiroshi Takaba[1]

[1]Faculty of Engineering, Gifu University, 1-1 Yanagido, Gifu, Gifu 501-1193, Japan; sudou@gifu-u.ac.jp
[2]Precursory Research for Embryonic Science and Technology (PRESTO), Japan Science and Technology Agency (JST), 4-1-8, Honcho, Kawaguchi, Saitama 332-0012, Japan; shiga_m@gifu-u.ac.jp
[3]Faculty of Science, Kagoshima University, 21-24 Korimoto, Kagoshima, Kagoshima 890-8580, Japan
omodaka@sci.kagoshima-u.ac.jp

Received July 21, 2017; accepted October 16, 2017

Abstract: H_2O maser emission at 22 GHz in the circumstellar envelope is one of the good tracers of detailed physics and kinematics in the mass loss process of asymptotic giant branch stars. Long-term monitoring of an H_2O maser spectrum with high time resolution enables us to clarify acceleration processes of the expanding shell in the stellar atmosphere. We monitored the H_2O maser emission of the semi-regular variable R Crt with the Kagoshima 6-m telescope, and obtained a large data set of over 180 maser spectra over a period of 1.3 years with an observational span of a few days. Using an automatic peak detection method based on least-squares fitting, we exhaustively detected peaks as significant velocity components with the radial velocity on a 0.1 km s^{-1} scale. This analysis result shows that the radial velocity of red-shifted and blue-shifted components exhibits a change between acceleration and deceleration on the time scale of a few hundred days. These velocity variations are likely to correlate with intensity variations, in particular during flaring state of H_2O masers. It seems reasonable to consider that the velocity variation of the maser source is caused by shock propagation in the envelope due to stellar pulsation. However, it is difficult to explain the relationship between the velocity variation and the intensity variation only from shock propagation effects. We found that a time delay of the integrated maser intensity with respect to the optical light curve is about 150 days.

Key words: masers — stars: individual (R Crateris) — stars: late type — stars: AGB and post-AGB — stars: outflows

1. Introduction

Understanding the mass loss process of the circumstellar envelope of asymptotic giant branch (AGB) stars is one of the long-standing issues both in the evolution of low mass stars and in the chemical evolution of matter in the Universe. It is generally accepted that the mass loss process in AGB stars is caused by radiation pressure on dust grains which launches the materials outwards (Höfner 2008, 2009). Recent high-resolution Atacama Large Millimeter/submillimeter Array (ALMA) observations have shown anisotropy of dust distribution such as clumpy structures (O'Gorman et al. 2014) and spiral structures (Decin et al. 2014). These facts indicate that the dust distribution is very complex and not always isotropic and homogeneous.

AGB stars often show the maser emission from SiO, H_2O, and OH molecules. Recent simultaneous observations of multi maser lines with the Korean VLBI Network telescopes showed the statistical properties of late evolutionary stages from AGB to post-AGB stars (Kim et al. 2014; Yoon et al. 2014; Kim et al. 2016). In particular, the H_2O maser emission at 22 GHz associated with the outer region of the dust shell is strongly affected by expanding motion of the envelopes and shock waves generated by the stellar pulsation. Thus, observations of the H_2O masers can be useful to trace the detailed motion of the materials in the envelope of stars undergoing loss of mass which was also revealed by some homogeneous databases provided by sensitive radio telescopes (e.g., Medicina 32m, Comoretto et al. 1990; Valdettaro et al. 2001).

The H_2O maser spectra show many velocity peaks, typically double peaks, due to Doppler shift which reflects the radial speed of the maser sources. By tracing the velocity in the H_2O maser spectra, we will be able to obtain information of the acceleration process in the envelope. Very-long-baseline interferometry (VLBI) mapping monitoring revealed that in some giant stars, the H_2O maser is distributed in the circumstellar shells with radii of several tens of AU. It has also indicated that it is accelerated up to velocities of ∼10 km s^{-1} by radiation pressure from the surrounding dust shell (Elizur 1992), and acceleration values are around the 0.1 km s^{-1} yr^{-1} level (e.g., Richards & Yates 1998).

Corresponding author: H. Sudou & M. Shiga

[†]The first two authors (HS and MS) equally contributed to this paper.

The semi-regular variable stars are known as a type of AGB stars and sometimes as H_2O maser emitters. They are good candidates for searching for the anisotropic property of the mass loss in the AGB phase, because they exhibit complex light variations. Although the origin of the irregularities is not clear, possible explanations include multi-periodic pulsations, non-radial oscillations, or the presence of a convection shell (Hinkle et al. 1997; Lebzelter et al. 2000 and references therein).

R Crt is a semi-regular variable classified as SRb of M7 spectral type (Kholopov et al. 1987). The V band magnitude varies with a pulsation period of 160 days as indicated in the American Association of Variable Star Observers (AAVSO) data base. The H_2O masers in R Crt show a double peak separated by 7 km s^{-1}, indicating that R Crt has typical maser spectral properties of AGB stars with expanding shells (Takaba et al. 1994). In particular, H_2O masers in R Crt have been examined intensively in order to study its velocity structure. VLBI monitoring during six months revealed the 3D velocity structure indicating a possible bipolar structure of the maser region with velocities ranging from 4.3 to 7.3 km s^{-1} (Ishitsuka et al. 2001, hereafter I01). Further, single-dish monitoring over 3 years showed complex velocity variability in the H_2O maser spectrum on the 0.1 km s^{-1} scale (Shintani et al. 2008). They also found switching between acceleration and deceleration in some velocity components, which can be evidence of periodic events and stellar pulsation. Although these observations advanced understanding of the dynamics of the envelope in R Crt, it is necessary to carry out more massive monitoring observation to understand the velocity variation in detail. In order to search for the complex velocity field in the circumstellar envelope in R Crt, we carried out frequent (once in few days) spectral monitoring of the H_2O maser with velocity resolution on the 0.1 km s^{-1} scale. Tracking velocity components by detecting all peaks in the maser spectra enables us to accurately monitor the activity of the circumstellar envelope in detail. We have exhaustively detected such all peaks using the code we developed for automatic peak detection based on a Gaussian basis function model.

2. OBSERVATIONS AND DATA REDUCTION

A time series of the H_2O maser spectra of R Crt at 22 GHz was observed over 1.3 years from January 2008 to March 2009, by using the 6-m telescope at Kagoshima, Japan (Omodaka et al. 1994). In total, we have obtained 187 maser spectra. This corresponds to an average observing frequency of once per few days. The digital spectrometer installed at the telescope has 160,000 channels, which provides 0.05 km s^{-1} per a channel, and the spectral range covered 64 MHz (830 km s^{-1}). The typical observation error of the velocity of the 6-m telescope is estimated to be 0.1 km s^{-1}, mainly limited by the accuracy of the velocity calibration for the Earth rotation parameters. The standard on-off beam-switching technique was used for observations of the source. System noise temperatures were measured at each observation and were used to correct the antenna temperature for atmospheric attenuation and changes in antenna gain as a function of the elevation angle. The typical error of the amplitude is estimated to be 10% in our R-sky calibration system of the 6-m telescope.

(a) Observed H_2O maser spectrum

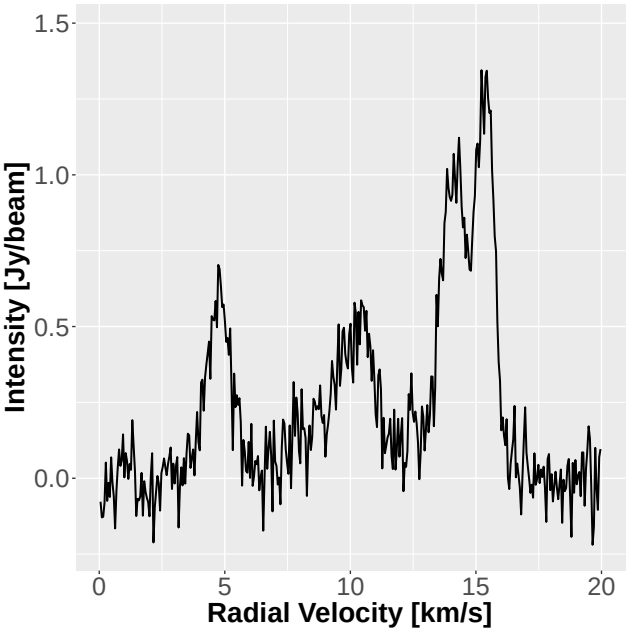

(b) Peak fitting result with Gaussian basis functions

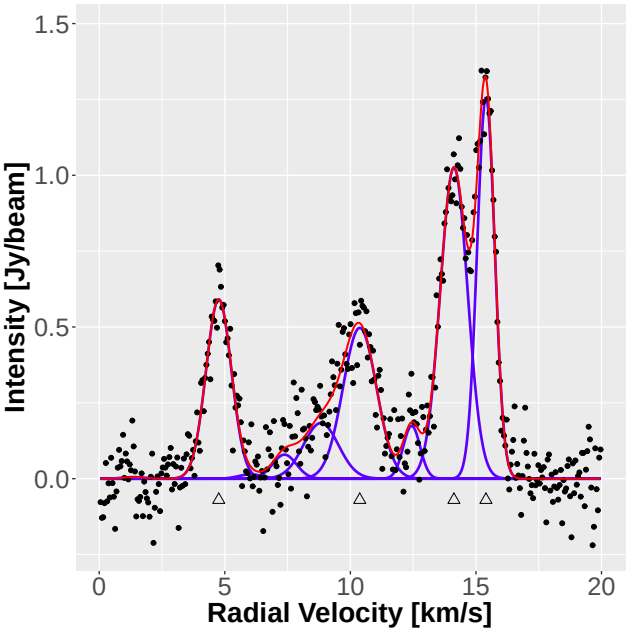

Figure 1. Typical spectra of H_2O maser emission in R Crt (observed on January 13, 2008) and fitting result. (a) Observed maser spectrum, in which the systemic velocity is 10.8 kms^{-1}. (b) Fitting result. Circles: observed data, red line: fitting result by equation (1), triangles: detected peaks (only significant components, $w_m \geq 0.3$) Jy/beam.

Figure 1(a) shows an example of the H_2O spectrum

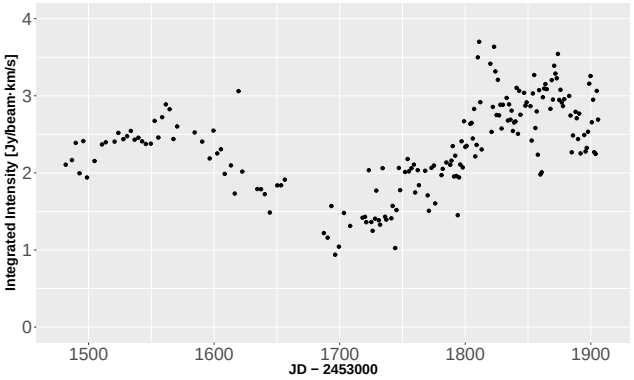

Figure 2. Time evolution of the integrated intensity.

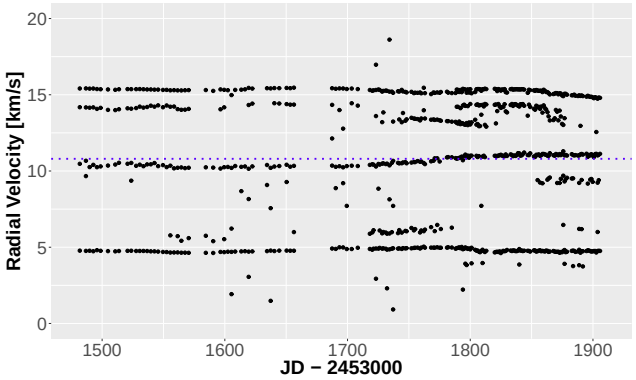

Figure 3. Time evolution of the fitted peak radial velocity covering the whole velocity range. The blue dotted line indicates the stellar velocity (10.8 km s^{-1}).

observed on January 13, 2008. This figure shows that there are several peaks in this spectrum. We found three main components; the components peaked around 10.8 km s^{-1}, which is the systemic velocity from the result of the CO observation profile (Bowers 1992), and those peaked around 5 and 15 km s^{-1}, which are blue-shifted and red-shifted components, respectively. The velocity distribution of these components is likely to be interpreted as a typical result from the expanding shell (I01).

Frequent monitoring over a long time period increases the size of spectral datasets to be analyzed. This makes manual analysis difficult because of the data analysis cost and human errors. Against this problem, automatic Gaussian deconvolution (AGD) algorithm, which is a fitting method with a Gaussian basis function model, was proposed in the massive 21-cm absorption survey (Lindner et al. 2015). The advantage of this approach is to automatically and exhaustively detect peaked components over entire observed spectra. Thus, this approach can drastically reduce both data analysis cost and human errors.

Peak detection by the AGD algorithm is implemented based on least-squares fitting with the basis function model. The algorithm initializes function parameters using several conditions with higher order derivatives and then optimizes function parameters by a gradient descent method. However this algorithm can fail to reach local optima to detect peaks correctly because it uses the initial parameters chosen by the proposed condition but it is still affected by observation noise. To avoid this problem, we took an approach that repeatedly and randomly initializes parameters presumed as peaked and then optimized parameters over all initial parameters, and finally chooses the best result minimizing the mean squared error (see Appendix in detail). After the optimization, less significant basis functions whose intensities are smaller than a threshold $w_{\rm thre}$ are removed from further analysis processes. Figure 1(b) shows an example of our result by the Gaussian basis function model with the threshold $w_{\rm thre} = 0.3$ Jy/beam and center positions of peaked components (basis functions) are indicated by symbol $\triangle$. This selection allows us to remove weak and short-lived components which are hard to identify at other observation dates. This figure shows that four bright peaks were detected by our method.

3. RESULTS

3.1. Time Series of the Integrated Intensity

Figure 2 shows the integrated total intensity for all detected components. The variability curves presented two clear peaks around JD = 2454560 and 2454870 during our monitoring period, and the separation of these peaks is about 300 days.

3.2. Time Series of the Peak Velocity of Each Maser Component

Figure 3 shows the time variations of the radial velocity of the detected peaks, ranging from 0 to 20 km s^{-1}. Some velocity components seem to have a lifetime of more than one year. These results are generally in agreement with previous work, which involved monitoring with the VLBI Exploration of Radio Astronomy (VERA) 25-m telescope in Iriki (Shintani et al. 2008). On the other hand, components with shorter lifetime seem to be more variable compared with blue- and red-shifted components. These highly variable components might be associated with irregular fluctuations in the envelope indicated by semiregular optical variations of the optical light curve in R Crt (Rudnitskij at al. 2010). In our present data, it is difficult to find the relationship between the velocity variation and optical variation, because our monitoring is not sensitive enough to trace the variation of these weak components correctly.

Figure 4 shows details of the time variations of blue-shifted, systemic, and red-shifted components, which lived for more than a year. In the blue-shifted components, we can find the velocity variations ranging $\pm$ 0.2 km s^{-1} (Figure 4a). The timescale of the variation is estimated very roughly from peak-to-peak measurements to be 300 days. This is very similar to the timescale of the variation of the integrated intensity shown in Figure 2. The red-shifted component is also likely to show similar velocity variation as that of the blue-shifted component. Its timescale is estimated

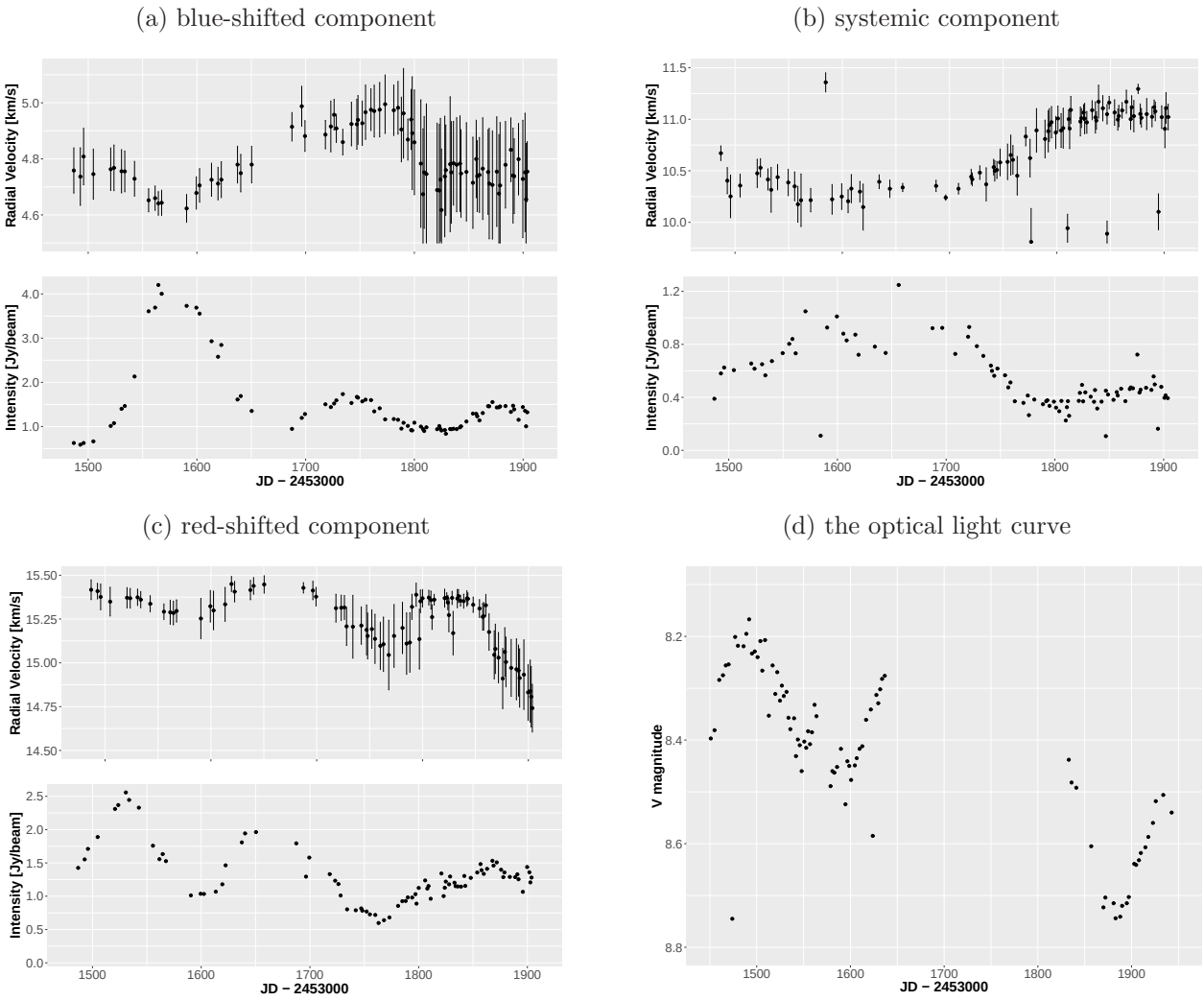

Figure 4. Time evolution of (a) blue-shifted component, (b) systemic component, and (c) red-shifted component. The top panel shows the radial velocity (circles) and the velocity width (bars), and the bottom panel shows the peak intensity of H_2O masers. (d) optical light by ASAS.

to be roughly 200 days. The timescale obtained in the flux monitoring of the optical and radio waves has been reported the periods of the AAVSO's optical light curve of 160 days and of the time variations of the OH masers in R Crt of 227 or 560 days (Etoka et al. 2001). It is unclear whether or not the timescale of the velocity variation is related to the optical and radio flux variations from our limited results.

The largest velocity shift can be seen in the systemic component. According to the simple expanding shell model, the shift of the radial velocity of the systemic components is expected to be very small, because they are expected to move to perpendicular to the line of sight. Similar behavior was reported in the previous paper of VLBI monitoring of R Crt (I01). They found that the largest velocity shift of ~ -4 km s^{-1} yr^{-1} was found for the components near the systemic velocity. Perhaps it is related to the bipolar flow in the H_2O maser shell suggested from the proper motion of the maser spots, or to the presence of non-radial oscillations.

We also show the time variation of the velocity dispersion of each component in Figure 4. The clear systematic variation of the velocity dispersion of the blue-shifted and red-shifted components cannot be found before JD = 2456500. Then the velocity dispersion becomes narrower from JD = 2454650 to 2454750, after that it becomes slightly wider. Although this tendency might show anti-correlation with intensity variations, further monitoring is needed to investigate it.

3.3. Time Series of the Peak Intensity of Each Maser Component

We show the light curve of R Crt obtained by the All Sky Automated Survey (ASAS, Pojmanski 1997) in Figure 4(d). Although it is remarkable that the big flare of the blue-shifted component can be seen near JD=2454550, corresponding to ~ 9 times the intensity just before the flare, there are no strong indications in the ASAS's optical light curve. The red-shifted component also showed similar but smaller flares near both

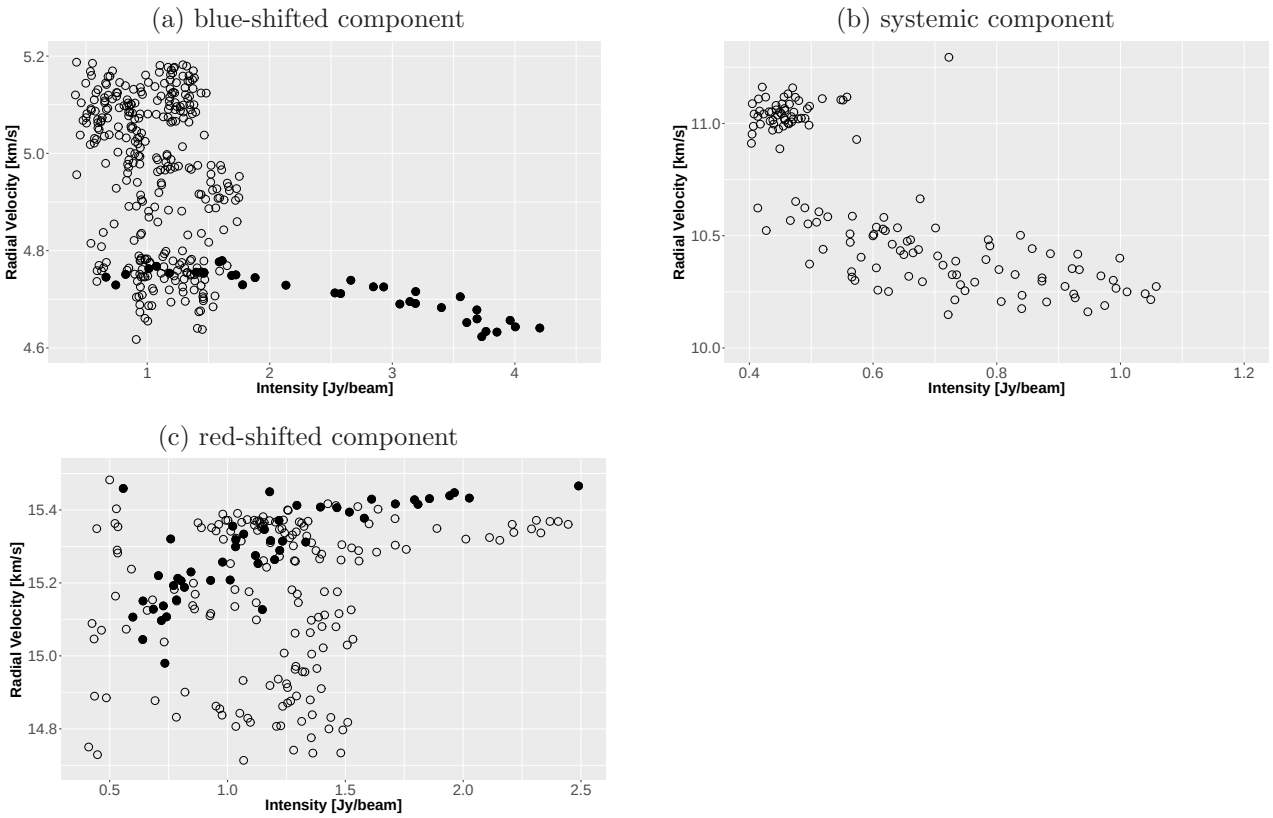

Figure 5. The correlation between the radial velocity and the intensity of the water maser. (a) blue-shifted component, (b) systemic component, and (c) red-shifted component. The open circles indicate the data in the whole observation period. The filled circles indicate the data obtained in the period of the flaring state between (a) JD=2454500 and 2454650, and (c) JD=2454600 and 2454770.

2454550 and 2454650 days. This fact indicates that the blue-shifted component is more active and variable compared with the red-shifted component during our monitoring. This activity might relate to the fact that the velocity variations for the blue-shifted component are almost twice as large as those for the red-shifted component (see Section 3.2).

It is known that intensity variations of masers are difficult to interpret because it relates to pumping mechanism such as heading and compression of the gas by shock (Gómez Balboa & Lepine 1986).

3.4. Correlation between Peak Velocity and Peak Intensity

Figure 5 shows the relationship between the radial velocity and the intensity of each component. Interestingly, it appears that the velocity variations are correlated with the intensity variations, that is, the expanding velocity increases (acceleration) with increasing intensity. Pearson correlation coefficient (cc) is -0.34 with p-value of 2.2×10^{-6} for the blue-shifted shown in Figure 5(a) and is 0.38 with p-value of 5.4×10^{-7} for red-shifted components in Figure 5(c). On the statistical hypothesis testing and the computation of p-values, the null hypothesis is that the two variables (intensity and velocity) are uncorrelated. Thus this analysis result shows the correlation between the acceleration and intensity enhancement (note that the negative correlation in the blue-shifted component means positive acceleration).

Further, by limiting the period of the flaring state of the maser features, we obtain a higher value of cc $= -0.87$ with p-value of 6.5×10^{-15} (JD=2454500 to 2454650, see Section 4.2) in the blue-shifted component, and 0.78 with p-value of 2.4×10^{-10} (JD=2454610 to 2454770, the second flare, see Section 4.2) in the red-shifted component, showing strong correlations during the flare states. On the other hand, the systemic component show strong correlation (cc $= -0.79$ with p-value of 9.9×10^{-41}) regardless of flare states.

4. DISCUSSION

4.1. Acceleration in the Maser Shell

It was known that R Crt emits SiO maser with a single peak, and both the H_2O and OH masers with a double peak separated by 7 and 17 km s^{-1}, respectively (Jewell et al. 1991; Dickinson & Chaisson 1973; Gómez Balboa et al. 1986; Etoka et al. 2001; Etoka et al. 2003; Kim et al. 2010). This fact indicates that materials are accelerated toward the outer region in the H_2O maser shell in the circumstellar envelope (Eliztur 1992). Averaged acceleration in the H_2O shell in R Crt can be estimated to be 0.4 km s^{-1} yr^{-1} from the measured shell size and velocity range under the assumption of the simple thin

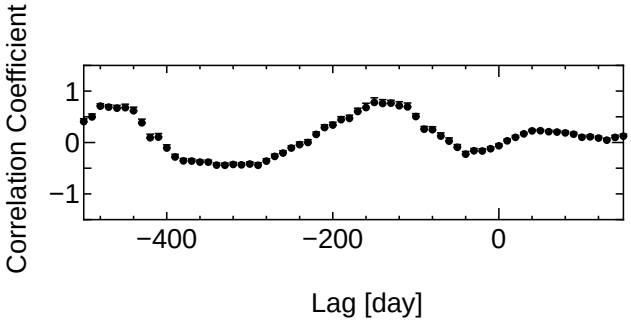

Figure 6. The discrete correlation function between the optical light curve and the integrated maser intensity. A negative lag means that variation of the maser is delayed with respect to that of the light curve.

shell model (I01). This value can be regarded as the averaged acceleration in the H_2O maser shell of R Crt, and is in good agreement with the typical acceleration obtained in the blue- and red-shifted components indicated from our observations.

In addition to linear acceleration, we found that the velocity change between acceleration and deceleration correlates slightly with the peak intensity of the maser for the first time (see Section 3.3). In order to explain the velocity variations in the stellar atmosphere of the AGB stars, a shock propagation model has been proposed (Wood 1979; Shintani et al. 2008). Based on this model, we propose a simple speculation for the origin of the change of acceleration. A shock wave is expected to be generated periodically by stellar pulsation and to propagate outward in the envelope. When the shock wave irrupts into the H_2O maser shell, it temporary causes both acceleration and intensity enhancement of the maser sources in the shell, if we take into account the collision pumping of the H_2O masers (Deguchi 1977). There after the shock wave passes through the H_2O maser shell, and the accelerated maser source becomes dark gradually. Then, the maser sources in the shell behind the shock are found to be relatively bright again. As a result, we observe apparent deceleration in the spectrum.

However, since the actual situation is likely to be more complex, it is not enough to consider only the shock propagation. We encounter difficulties because (1) acceleration without the intensity variation was sometimes observed, and (2) the mechanism of the maser excitation or the intensity amplification is generally very complex because of beaming effect of maser emission. Further, (3) VLBI mapping observations showed that an H_2O maser feature sometimes exhibits complex spatial and velocity structure, and the structure can easily change on the timescale of the order of a few months (e.g., Sudou et al. 2002), and (4) the observed velocity shift might not reflect the real bulk motion of the masers (e.g., Imai et al. 1997). We also cannot reject any other possibilities that the velocity shift is due to non-radial motion, such as a bipolar flow, because the presence of the bipolar flow is implied

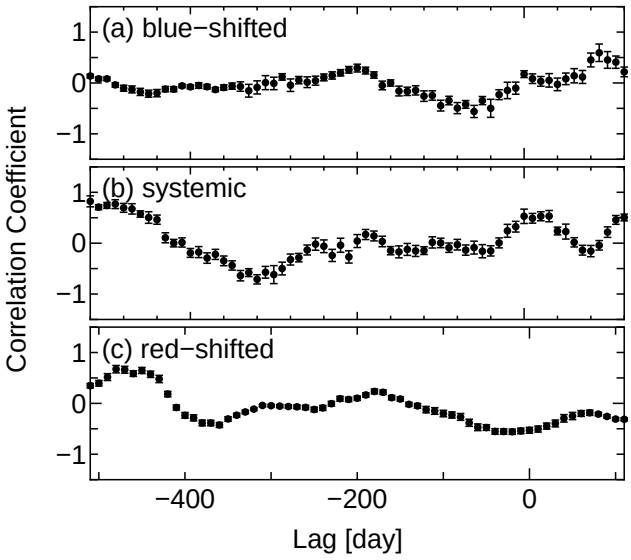

Figure 7. The discrete correlation function between the optical light curve and the maser intensity. A negative lag means that variation of the maser is delayed with respect to that of the light curve.

by using the proper motion of the H_2O maser features (I01).

It follows from that we need to obtain further data sets of the H_2O spectrum including the proper motion with VLBI as well as the other maser lines in R Crt (e.g., SiO and OH). Detailed 3-D motion and acceleration will be very useful to understand the shock propagation effect, and to incorporate the radiative transfer process in the envelope in order to understand dust-driven wind (e.g., Khouri et al. 2015).

4.2. Relationship between Light Curve and Maser Variability

The light curve of R Crt obtained by ASAS shows that the optical main period is estimated to be $P \sim 474$ days, which is 3 times longer than the timescale of the period of 160 days suggested from AAVSO. We carried out a cross correlation analysis between the maser integrated intensity and the light curve in Figure 6 by using the discrete correlation function introduced for unevenly sampled data (Edelson & Krolik 1988). We found the maximum correlation between them at a lag time of 150 day with cc = 0.78. This corresponds to 0.3 P for $P = 474$ days. The secondary correlation peak can be seen at a lag time of 480 day with cc = 0.71. In some supergiants, similar correlations have been reported by using light curves with longer periods up to 20 years (e.g., Lekht et al. 2001, 2005, Rudnitskij 2005). They estimated the lag time to be 0.05 – 0.5 P. On the other hand, no correlation was also reported from the data of a semi-regular variable RX Boo over 6 years (Winnberg et al. 2008). They suggested that the variation of the maser intensity could be due to the turbulence of the velocity coherence length of H_2O maser amplification.

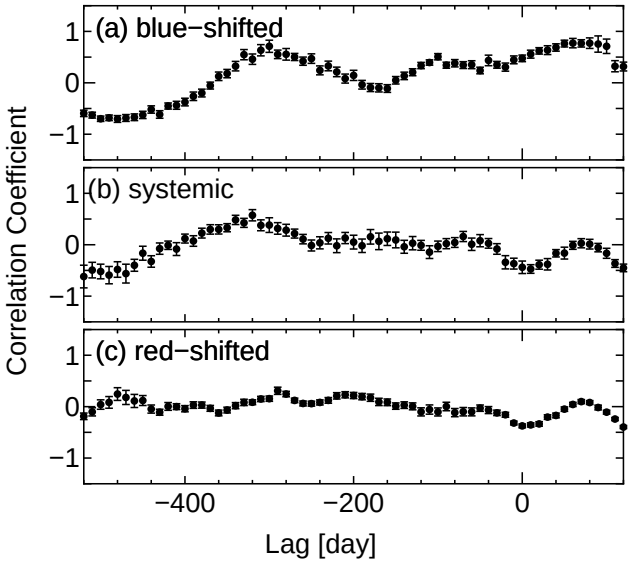

Figure 8. The discrete correlation function between the optical light curve and the maser velocity. A negative lag means that variation of the maser is delayed with respect to that of the light curve.

We conducted the same analysis between both the intensity and velocity for each maser component and the light curve, and we did not find a found clear correlation between them with the lag time smaller than P (see Figures 7 and 8). The tight correlation between the optical variation and the velocity variation of high-excitation CO lines formed much closer to the star than H_2O maser lines has been found in semi-regular variables on the 1 – 10 km s^{-1} scale (Lebzelter et al. 2000). Our present monitoring span of the water maser in R Crt of 1.3 year is much shorter than that of the optical light curve with ASAS ($\sim$ 9 years).

5. CONCLUSION

The H_2O maser spectra of a semi-regular variable R Crt were monitored in the radial velocity on the 0.1 km s^{-1} scale and peaked components in the radial velocity were exhaustively detected using our newly developed automatic method. The blue-shifted and red-shifted components exhibited switching between acceleration and deceleration. This velocity variation correlates with the intensity variation with the correlation coefficient of ~ 0.4, in particular during the flaring state of the water maser with the correlation coefficient of $\sim 0.8 - 0.9$. These facts can be explained by the idea that the shock propagation due to the pulsation makes the maser sources brighten and accelerate simultaneously. However, this implication is not enough to explain the relationship between the maser intensity and velocity simply, because the mechanism of the maser excitation and acceleration is certainly more complex. To support this idea, it is important to continue to frequently measure the velocity variation for longer periods by using occupied single dishes and to analyze such massive monitoring datasets along with long-term optical monitoring.

ACKNOWLEDGMENTS

We would like to thank the anonymous referees, who gave us many useful comments that improved the paper very much. We also thank Takeru Suzuki, Yuki Yasuda, Ryota Inaba, and Yuna Morishima for helpful conversations. This work is in part supported by JSPS KAKENHI (Grant-in-Aid for Scientific Research) #25870322, #16H02866 and JST PRESTO #JPMJPR16N6.

REFERENCES

Bowers, P. F. 1992, Location of the Dust Formation Region for Mira Variables, ApJ, 390, L27

Comoretto, G., Palagi, F., Cesaroni, R., Felli, M., Bettarini, A., et al. 1990, The Arcetri Atlas of H_2O Maser Sources, A&AS, 84, 179

Decin, L., Richards, A. M. S., Neufeld, D., Steffen, W., Melnick, G., & Lombaert, R. 2015, ALMA Data Suggest the Presence of Spiral Structure in the Inner Wind of CW Leonis, A&A, 574, 5

Deguchi, S. 1977, Water Maser and Envelope of Infrared Stars, PASJ, 29, 669

Dickinson, D. F., & Chaisson, E. J. 1973, Long-Period Variables: Correlation of Stellar Period with OH Radial-Velocity Pattern, ApJ, 181, L135

Edelson, R. A., & Krolik, J. H. 1988, The Discrete Correlation Function - A New Method for Analyzing Unevenly Sampled Variability Data, ApJ, 333, 676

Elitzur, M. 1992, Astronomical Masers, ARA&A, 30, 75

Etoka, S., Blaszkiewics, L., Szymczak, M., & Le Squeren, A. M. 2001, Monitoring of Long Term Behaviour of OH Masers in Semiregular Variables: R Crt, W Hya and RT Vir, A&A, 378, 522

Etoka, S., Le Squeren, A. M., & Gerard, E. 2003, Detection of 1612 MHz OH Emission in the Semiregular Variable Stars RT Vir, R Crt and W Hya, A&A, 403, L51

Gómez Balboa, A. M., & Lepine, J. R. D. 1986, Time Variation of the H_2O and SiO Masers in Late-Type Stars, A&A, 159, 166

Hinkle, K. H., Lebzelter, T., & Scharlach, W. W. G. 1997, Infrared Velocities of Long Period Variables: CO Δv=3 in Four Miras and Five SR Variables, AJ, 114, 2686

Höfner, S. 2008, Winds of M-Type AGB Stars Driven by Micron-Sized Grains, A&A, 491, L1

Höfner, S. 2009, Dust Formation and Winds around Evolved Stars: The Good, the Bad and the Ugly Cases, in Cosmic Dust – Near And Far, (ed.) T. Henning, E. Grün, & J. Steinacker (Heidelberg: ASP), 414, 3

Imai, H., Shibata, K. M., Sasao, T., Miyoshi, M., Kameya, O., et al. 1997, Measurement of Shifts in Line-Of-Sight Velocities of Stellar Water Masers Using VLBI, A&A, 319, L1

Ishitsuka, J. K., Imai, H., Omodaka, T., Ueno, M., Kameya, O., et al. 2001, VLBI Monitoring Observations of Water Masers around the Semi-Regular Variable Star R Crateris, PASJ, 53, 1231 (I01)

Jewell, P. R., Snyder, L. E., Walmsley, C. M., Wilson, T. L., & Gensheimer, P. D. 1991, Observational Properties of $V = 1$, $J = 1$ - 0 SiO Masers, A&A, 242, 211

Kholopov, P. N., Samus, N. N., Durlevich, O. V., Kazarovets, E. V., Kireeva, N. N., & Tsvetkova, T. M.

1987, (4th ed.) The 68th Name-List of Variable Stars, General Catalogue of Variable Stars (Moscow: Nauka)
Khouri, T., Waters, L. B. F. M., de Koter, A., Decin, I., Min, M., de Vries, B. L., Lombert, R., & Cox, N. L. J. 2015, Dusty wind of W Hydrae. Multi-Wavelength Modelling of the Present-Day and Recent Mass Loss, A&A, 577, 114
Kim, J., Cho, S.-H., & Kim, S. J. 2010, Simultaneous Observations of SiO and H_2O Masers toward Known Stellar H_2O Maser Sources, AJ, 145, 22
Kim, J., Cho, S.-H., & Kim, S. J. 2014, Statistical Studies Based on Simultaneous SiO and H_2O Maser Surveys toward Evolved Stars, AJ, 147, 22
Kim, J., Cho, S.-H., & Yoon, D.-H. 2016, Monitoring Observatinos of H_2O and SiO Masers Toward Post-AGB Stars, JKAS, 49, 261
Lebzelter, T., Kiss, L. L., & Hinkle, K. H. 2000, A Comparison of Light and Velocity Variations in Semiregular Variables, A&A, 361, 167
Lekht, E. E., Mendoza-Torres, J. E., Rudnitskij, G. M., & Tolmachev, A. M. 2001, Variability of the H_2O Maser Associated with the Mira Variable RS Virginis, A&A, 376, 928
Lekht, E. E., Rudnitskij, G. M., Mendoza-Torres, J. E., & Tolmachev, A. M. 2005, Variability of the H_2O Maser Associated with the M-Supergiant S Persei, A&A, 437, 127
Lindner, R. R., Vera-Ciro, C., Murray, C. E., Stanimirović, S., et al. 2015, Autonomous Gaussian Decomposition, ApJ, 149, 138
O'Gorman, E., Vlemmings, W., Richards, A. M. S., Baudry, A., De Beck, E., et al. 2015, ALMA Observations of Anisotropic Dust Mass Loss in the Inner Circumstellar Environment of the Red Supergiant VY Canis Majoris, A&A, 573, L1
Omodaka, T., Morimoto, M., Kawaguchi, N., Kitamura, Y., Tanaka, M., et al. 1994, The 6m mm-VLBI Telescope at Kagoshima; Japan, Astronomy with Millimeter and Submillimeter Wave Interferometry, IAU Colloq. 140, ed. M. Ishiguro & J. Welch (San Francisco: ASP), 64
Pojmanski, G. 1997, The All Sky Automated Survey, Acta Astron., 47, 467
Richards, A. M. S., & Yates, J. A. 1998, Maser Mapping of Dust-Driven Winds from Red Supergiants, Irish Astronomical Journal, 25, 7
Rudnitskij, G. M. 2005, Monitoring of Spectral Variations of Mira-Type and Semiregular Variable Stars, Odessa Astronomical Publications, 18, 90
Rudnitskij, G. M., Pashchenko, M. I., & Colom, P. 2010, Polarization Observations of Circumstellar OH Masers, Astronomy Reports, 54, 400
Shintani, M., Imai, H., Ando, K., Nakashima, K., Hirota, T., et al. 2008, Statistical Properties of Stellar H_2O Masers — Results of Three-Year Single-Dish Observations with the VERA Iriki Telescope, PASJ, 60, 1077
Sudou, H., Omodaka, T., Imai, H., Sasao, T., Takaba, H., Nishio, M., Hasegawa, W., & Nakajima, J. 2002, VLBI Observations of Water Masers in the Circumstellar Envelope of IRC+60169, PASJ, 54, 757
Szymczak, M., & Le Squeren, A. M. 1999, A Comparison of OH and H_2O Maser Properties of Mira and Semiregular Variable Stars, MNRAS, 304, 415
Takaba, H., Ukita, N., Miyaji, T., & Miyoshi, M. 1994, Spectral Evolution of the $H2_O$ Maser in Late-Type Stars, PASJ, 46, 629
Valdettaro, R., Palla, F., Brand, J., Cesaroni, R., Comoretto, G., et al. 2001, The Arcetri Catalog of H_2O Maser Sources: Update, 2000, A&A, 368, 845
Yoon, D.-H., Cho, S.-H., Kim, J., Yun, Y. J., & Park, Y.-S. 2014, SiO and H_2O Maser Survey toward Post-Asymptotic Giant Branch and Asymptotic Giant Branch Stars, ApJS, 211, 15
Winnberg, A., Engels, D., Brand, J., Baldacci, L., & Walmsley, C. M. 2008, Water Vapour Masers in Long-Period Variable Stars. I. RX Bootis and SV Pegasi, A&A, 482, 431
Wood, P. R. 1979, Pulsation and Mass Loss in Mira Variables, ApJ, 227, 220

APPENDIX A. AUTOMATIC PEAK DETECTION

Our developed peak detection method is based on a least squares fitting of a Gaussian basis function model. After the model is fitted to an observed maser spectrum, peaks are given by the center positions of the optimized basis functions. This section describes our method, which consist of the assumed model, optimization algorithm of model parameters and peak detection procedure.

Appendix A.1. Peak Modelling with Gaussians

Let x_n be the n-th observed value of velocity and y_n be the observed intensity at velocity x_n. Because the observed y can be negative due to observation noise, we replaced all negative values of y with zeros. All values of x and y are vectorized as $\boldsymbol{x} = (x_1, \ldots, x_N)^{\mathrm{T}}$ and $\boldsymbol{y} = (y_1, \ldots, y_N)^{\mathrm{T}}$, where N is the number of discretized velocity values. Then an observed spectrum consists of the pair of $\boldsymbol{x}$ and $\boldsymbol{y}$.

As shown in figure 1(a), each peaked component has symmetric and exponentially decreasing components around the peak, which looks like a Gaussian function. Our model approximates a peaked velocity component by a Gaussian basis function:

$$\phi(x; \mu, \sigma) = \exp\left(-\frac{(x-\mu)^2}{2\sigma^2}\right), \tag{1}$$

where μ is the center and σ is the dispersion of the component. And then the intensity of a maser spectrum at x_n is approximated by a linear combination of Gaussian basis functions:

$$\hat{y}_n = \sum_{m=1}^{M} w_m \phi(x_n; \mu_m, \sigma_m) = \boldsymbol{w}^{\mathrm{T}} \boldsymbol{\phi}(x_n), \quad n = 1, \ldots, N \tag{2}$$

where M is the number of basis functions, $\boldsymbol{w} = (w_1, \ldots, w_M)^{\mathrm{T}}$ are parameters of a non-negative weight vector and $\boldsymbol{\phi}(x_n) = \Big(\phi(x_n; \mu_1, \sigma_1), \ldots, \phi(x_n; \mu_M, \sigma_M)\Big)^{\mathrm{T}}$ is a vector consisting of M Gaussian basis functions.

Each basis function ϕ_m has three parameters, *i.e.* weight (height) w_m, center location μ_m, and dispersion (variance) σ_m^2, and then the model totally have $3 \times M$ parameters; $\boldsymbol{\theta} = (\boldsymbol{w}, \boldsymbol{\mu}, \boldsymbol{\sigma})$, to be optimized based on least squares fitting to an observed spectrum. M is

also a parameter but this cannot be optimized from an observed spectrum because increasing M causes overfitting. We first examined all the spectra and then we manually set $M = 10$ in our data analysis. Roughly choosing the value of M does not cause an incorrect result because the weight parameters of unnecessary components tend to be small values and some of the components located close each other were removed in our post-processing procedure.

Appendix A.2. Parameter Optimization Algorithm

A least squares fitting is a parameter optimization based on minimizing the squared error between observed values and estimated values:

$$J(\boldsymbol{\theta}) = \frac{1}{2}\sum_{n=1}^{N}\left\{y_n - \boldsymbol{w}^{\mathrm{T}}\boldsymbol{\phi}(x_n)\right\}^2. \tag{3}$$

In our problem setting, the optimization problem for all parameters $\boldsymbol{\theta}$ is non-convex, where there are many local optima. Our algorithm first initialize parameters and then iteratively optimizes each parameter one-by-one with certain fixed parameters until convergence. This procedure is repeatedly implemented from different initial parameters. Among optimization results from different initializations, the best model minimizing $J(\boldsymbol{\theta})$ is chosen as the final fitting result. The reminder of this section presents an optimization of each parameter, an initialization procedure, and a post-processing procedure to remove redundant components.

Optimization of $\boldsymbol{w}$: With fixed $\boldsymbol{\mu}$ and $\boldsymbol{\sigma}$, the error function $J(\boldsymbol{w})$ is a quadratic convex function regarding to $\boldsymbol{w}$. Thus using the equation $\frac{\partial}{\partial \boldsymbol{w}}J(\boldsymbol{w}) = 0$, the optimal $\boldsymbol{w}$ can be analytically computed by

$$\boldsymbol{w} = (\boldsymbol{\Phi}^{\mathrm{T}}\boldsymbol{\Phi})^{-1}\boldsymbol{\Phi}^{\mathrm{T}}\boldsymbol{y}, \tag{4}$$

where

$$\boldsymbol{\Phi} = \begin{pmatrix} \phi(x_1;\mu_1,\sigma_1) & \phi(x_1;\mu_2,\sigma_2) & \dots & \phi(x_1;\mu_M,\sigma_M) \\ \phi(x_2;\mu_1,\sigma_1) & \phi(x_2;\mu_2,\sigma_2) & \dots & \phi(x_2;\mu_M,\sigma_M) \\ \vdots & \vdots & \ddots & \vdots \\ \phi(x_N;\mu_1,\sigma_1) & \phi(x_N;\mu_2,\sigma_2) & \dots & \phi(x_N;\mu_M,\sigma_M) \end{pmatrix}. \tag{5}$$

After updating $\boldsymbol{w}$ using equation (4), the elements of $\boldsymbol{w}$ can be negative. Thus, our algorithm replaces all negative values in $\boldsymbol{w}$ with zeros after the update (4).

Optimization of $\boldsymbol{\mu}$ and $\boldsymbol{\sigma}$: The error functions of $\boldsymbol{\mu}$ and $\boldsymbol{\sigma}$ are not quadratic convex functions, such that the optimal parameter cannot be computed analytically. Our method used a gradient descend approach to optimize these parameters, which is given by

$$\boldsymbol{\mu} \leftarrow \boldsymbol{\mu} - \eta\frac{\partial J(\boldsymbol{\theta})}{\partial \boldsymbol{\mu}} \tag{6}$$

$$\boldsymbol{\sigma} \leftarrow \boldsymbol{\sigma} - \eta\frac{\partial J(\boldsymbol{\theta})}{\partial \boldsymbol{\sigma}},. \tag{7}$$

η is s step size to be set to a small enough value ($\eta = 10^{-3}$ in our experiment) and

$$\frac{\partial J(\boldsymbol{\theta})}{\partial \boldsymbol{\mu}} = \left(\frac{\partial J(\boldsymbol{\theta})}{\partial \mu_1},\dots,\frac{\partial J(\boldsymbol{\theta})}{\partial \mu_M}\right)^{\mathrm{T}}, \tag{8}$$

$$\frac{\partial J(\boldsymbol{\theta})}{\partial \boldsymbol{\sigma}} = \left(\frac{\partial J(\boldsymbol{\theta})}{\partial \sigma_1},\dots,\frac{\partial J(\boldsymbol{\theta})}{\partial \sigma_M}\right)^{\mathrm{T}}. \tag{9}$$

In the update rule, the first derivatives are computed by

$$\frac{\partial J}{\partial \mu_m} = \sum_{n=1}^{N}\left\{y_n - \sum_{j=1}^{M} w_j \exp\left(-\frac{(x_n-\mu_j)^2}{2\sigma_j^2}\right)\right\} \left\{-\frac{w_m(x_n-\mu_m)}{\sigma_m^2}\exp\left(-\frac{(x_n-\mu_m)^2}{2\sigma_m^2}\right)\right\} \tag{10}$$

$$\frac{\partial J}{\partial \sigma_m} = \sum_{n=1}^{N}\left\{y_n - \sum_{j=1}^{M} w_j \exp\left(-\frac{(x_n-\mu_j)^2}{2\sigma_j^2}\right)\right\} \left\{-\frac{w_m(x_n-\mu_m)^2}{\sigma_m^3}\exp\left(-\frac{(x_n-\mu_m)^2}{2\sigma_m^2}\right)\right\}. \tag{11}$$

Our optimization updates these parameters $\boldsymbol{w}$, $\boldsymbol{\mu}$ and $\boldsymbol{\sigma}$ alternately until convergence.

In this optimization, initializing the center parameter $\boldsymbol{\mu}$ is essentially important to reach to a good local optimum for an appropriate fitting result. To choose an appropriate initialization of $\boldsymbol{\mu}$, we implemented the following procedure: we first set the threshold value h_{noise} ($h_{\mathrm{noise}} = 0.1$ Jy/beam in our experiment) to remove observation noise, and then listed all position x_n whose output y_n is greater than h_{noise}. Next we randomly select a position x from the list and set to an initial value of center μ_1. Then the selected value and the values whose distance from the selected value is less than h_{dist} ($h_{\mathrm{dist}} = 0.1$ kms^{-1} in our experiment) are removed from the list. The next initial value of μ_2 is then randomly chosen from the list. This procedure is iterated until the number of selected centers reaches to M. Due to the threshold h_{dist}, the list can be empty after some initial positions are chosen. In this case, the value of h_{dist} decreased to the half, *i.e.* $h_{\mathrm{dist}}/2$, and the initialization procedure continues.

After optimizing the parameters, the centers of the basis functions can be similar. As a post-processing procedure, our method chooses only the basis function with larger weight parameter w from close basis functions (for which the distance between the centers is less than 0.5) and removes the other basis function. Then the parameters are optimized again. Even after our optimization, there can be several small components because of observation noise. Since the observed spectrum features with low signal-to-noise ratio hard to be decomposed correctly due to blending effect of complex features, we removed components with $w_m \leq w_{\mathrm{thre}}$, which each spectral feature to be almost negligible compared with the observation errors. Then our method outputs the center of the remaining basis functions as peak positions in the observed spectrum.